Geochemistry, Geophysics, Geosystems®

AGU ADVANCING EARTH AND SPACE SCIENCES

RESEARCH ARTICLE
10.1029/2023GC010989

**Key Points:**

- Fine grained siderites with a limited amount of ferric iron sorbed onto them were synthesized
- Warming curves of 5 K remanences of these siderites show a tail beyond its nominal Néel temperature, an effect of the surface coating
- Fine grained siderite can be detected down 0.1 wt% by processing field-cooled warming curves

**Supporting Information:**

Supporting Information may be found in the online version of this article.

**Correspondence to:**

M. J. Dekkers,
m.j.dekkers@uu.nl

**Citation:**

Dekkers, M. J., Hanckmann, W., Spassov, S., & Behrends, T. (2023). Low temperature magnetic properties of variably oxidized natural and synthetic siderite. *Geochemistry, Geophysics, Geosystems*, *24*, e2023GC010989. https://doi.org/10.1029/2023GC010989

Received 4 APR 2023
Accepted 30 AUG 2023



# Low Temperature Magnetic Properties of Variably Oxidized Natural and Synthetic Siderite

**Mark J. Dekkers[1], Wout Hanckmann[1], Simo Spassov[2], and Thilo Behrends[1]**

[1]Department of Earth Sciences, Utrecht University, Utrecht, The Netherlands, [2]Geophysical Centre of the Royal Meteorological Institute of Belgium, Dourbes, Belgium

**Abstract** Siderite ($FeCO_3$) is an important ferrous iron carbonate in the geochemical cycling of iron, as it is a sink for iron under reducing conditions. However, its detection is not straightforward with classical analytical approaches because in natural samples it is often fine-grained and/or occurs in low concentrations. In this study, we explore the analytical potential of low-temperature magnetometry. Synthetic siderites with a limited amount of associated ferric iron of up to 5 mol% and some natural siderites were subjected to investigation. Maxima in the cooling curves in a 5 T magnetic field shows that the Néel temperature of siderite is at 37 K in agreement with literature data. Those maxima appear at a higher temperature in the synthetic siderites with associated/sorbed ferric iron; it is 45 K for the 5 mol% $Fe^{3+}$ synthesis. With the increasing amount of ferric iron, the synthetic siderites show an increasingly prominent remanence tail beyond the nominal Néel temperature in field-cooled (FC) and zero-field-cooled (ZFC) warming curves of the remanent magnetization acquired in 5 T at 5 K. Fine-grained siderite alters in air on laboratory time scales which is manifested by more pronounced remanence tails up to higher temperatures. Siderite's presence is best diagnosed by evaluating a combination of FC warming curves and a FC/ZFC remanence ratio >3 at 5 K. Standard addition experiments of FC warming curves enable the determination of siderite down to 0.1 wt%.

**Plain Language Summary** Siderite ($FeCO_3$) is a foremost reservoir of iron, an important biogeochemical element, in sediments under reducing conditions. Therefore, determining how much siderite is present in a sediment is important but not so straightforward: X-ray diffraction (XRD) is not that sensitive when dealing with fine particles, siderite's typical mode of occurrence. Here, we explore the analytical potential of low-temperature magnetometry (a sensitive technique) by taking advantage of the magnetic properties of siderite. We document siderite's magnetic properties in the 4–300 K temperature range by studying several synthetic siderites that contain up to a few percentage of associated or sorbed ferric iron and some natural siderites. The temperature below which siderite becomes magnetic, the Néel temperature nominally at 37 K, rises with the ferric iron amount, while exposure to air also rises the temperature, hinting at the development and growth of a surface coating. Low-temperature magnetometry enables detection of siderite down to 0.1%, that is, the technique is much more sensitive than XRD.

## 1. Introduction

Siderite ($FeCO_3$) is an important diagenetic mineral in the geochemical cycling of iron, both in terrestrial and marine settings. It occurs as concretions and in disseminated form. It is often co-occurring with other carbonates such as calcite ($CaCO_3$), dolomite ($CaMg(CO_3)_2$), rhodochrosite ($MnCO_3$); (partial) solid solutions of these minerals with siderite may occur as well (e.g., Postma, 1981; Saunders & Swann, 1992; Sitko et al., 2009). Siderite forms in anoxic non-sulfidic environments in which iron oxides dissolve (Poulton & Canfield, 2005; Roberts, 2015). In sufficiently organic-rich sediments, organic matter degradation produces high $CO_2$ levels while the reduction of iron(oxy) (hydr)oxides yields ferrous iron which creates favorable conditions for early diagenetic siderite formation. Even at low concentrations, siderite often controls the availability of iron in ground waters, while its dissolution or precipitation provides a source or sink for contaminants (e.g., Guo et al., 2007; Jönsson & Sherman, 2008). Therefore, means to establish siderite's presence and concentration are required. However, its determination may be tedious, particularly for the typically prevailing low concentrations in many rocks. Next to the classical determination with X-ray diffraction (XRD) techniques (which feature a relatively high limit of detection, especially for poorly crystalline material), it is often determined geochemically in an operationally defined manner through sequential extraction schemes. Such schemes are tailored to the sediment under investigation (e.g., Claff et al., 2010; Morera-Chavarría et al., 2016; Poulton & Canfield, 2005). Sequential

extraction techniques may also show higher and/or faster dissolution for fine-grained poorly crystalline material than for the standards that are typically being used to calibrate the methods. Thus, while the approach is perfectly reproducible, iron pools may be allocated to different phases than would follow from the standards. Focusing on siderite, a way to sense siderite directly as a mineral phase is highly desired. Here, we explore a mineral magnetic approach to detect and quantify siderite making use of its magnetic ordering temperature of ∼37 Kelvin (K) (e.g., Frederichs et al., 2003; Jacobs, 1963) and its permanent magnetic signal below that temperature. The ordering temperature is a Néel temperature because siderite is an antiferromagnet below 37 K. Mineral magnetic characterization techniques are attractive because magnetic minerals can be sensed down to very low concentrations, and the detection limit is distinctly lower than that of XRD or Moessbauer spectroscopy. Despite their sensitivity, mineral magnetic techniques are not often employed to detect siderites primarily because low-temperature instrumentation is required to detect siderite's magnetism below its Néel temperature. One of the few examples include Housen et al. (1996), who determined siderite in subduction channel chalk sediments drilled in the Barbados accretionary prism (Atlantic Ocean, ODP Leg 156) by making use of siderite's Néel temperature. They utilized low-temperature magnetometry; XRD on magnetic concentrates served to confirm the presence of siderite.

In addition to its geochemical significance, siderite is important for paleomagnetism as its oxidation products, iron(oxy)(hydr)oxides, can acquire a secondary natural remanent magnetization, complicating paleomagnetic interpretation of siderite- and former-siderite-bearing strata (Ellwood et al., 1986; Hirt & Gehring, 1991; Hus, 1990). While coarse grained siderite is stable over geological time scales, fine grained siderite oxidizes depending on its grain size (e.g., Seguin, 1966). Fine-grained siderite-bearing chalks change their magnetic properties over the course of several weeks to months (Ellwood et al., 1986). Hus (1990) and Hirt and Gehring (1991) performed heating experiments on siderite-bearing sediments documenting siderite changing to magnetite and hematite depending on the heating temperature. Despite this potential paleomagnetic relevance, the magnetic properties of siderite are poorly known, making the determination of siderite by magnetic means currently rather tedious. The mineral magnetic approaches work only below the Néel temperature (∼37 K for siderite) and are often non-unique. Low-temperature magnetic properties of rhodochrosite ($MnCO_3$) may be confused with those of siderite upon cursory magnetic examination (Frederichs et al., 2003). Therefore, robust magnetic information unambiguously associated to siderite, is required for its identification in natural samples.

The properties of magnetic iron sulfides, such as monoclinic and hexagonal pyrrhotite, $Fe_7S_8$ (4 M polytype) and $Fe_9S_{10}$-$Fe_{11}S_{12}$ (1 T, 3 T, 4 H, 5 T, 6 T, and 7 T polytypes, cf. JCPDS–International Centre for Diffraction Data, 1993), are also superficially similar to those of siderite. Monoclinic pyrrhotite shows a magnetic transition at 30–34 K (Fillion & Rochette, 1988; Rochette et al., 1990) that may be confused with the Néel temperature of siderite in warming curves of low-temperature laboratory-induced remanences (Housen et al., 1996). Hexagonal pyrrhotites are antiferromagnetic, so magnetic pyrrhotite is traditionally equated to 4 M pyrrhotite. However, it was recently demonstrated that the 3 T polytype is ferrimagnetic, complicating the interpretation of low-temperature magnetometry of pyrrhotite (Horng, 2018; Horng & Roberts, 2018). Greigite ($Fe_3S_4$) and to a lesser extent smythite ($Fe_9S_{11}$) can also be confused with pyrrhotite (Horng, 2018; Horng & Roberts, 2018; Horng et al., 2020) and thus with siderite. This illustrates that care should be taken when assigning certain behaviors to siderite other options should be explicitly excluded. Erroneous attribution to siderite instead of so-called acid volatile sulfides (AVS: amorphous FeS, tetragonal $FeS_{1-x}$, and greigite lumped together) has also been reported when the Poulton-Canfield sequential extraction scheme was applied to AVS-rich sediments from the Black Sea and the Gulf of Bothnia (Egger et al., 2015). Additionally, fine-grained siderite is geochemically unstable under oxic conditions and thus may oxidize rapidly, at laboratory time scales.

While siderite contains nominally only ferrous iron, incorporation/sorption of some ferric iron might be possible in the initial state of the slow oxidation process ultimately to iron(oxy)(hydr)oxides. Therefore, we synthesize siderite under controlled redox conditions. Incipient oxidation of siderite may change its magnetic properties in comparison to "standard" coarse grained well-crystalline siderite. We first provide a brief overview of siderite's magnetic properties, followed by a report on the magnetic properties of the synthesized siderite along with those of some natural siderites. We show that siderite can be straightforwardly detected down 0.1 wt% with magnetic approaches.

## 2. Magnetism of Siderite

Siderite's specific density is 3,960 kg/m$^3$ (Hurlbut, 1971). It is trigonal with unit cell parameters a = 4.6916 Å and c = 15.3796 Å (space group $R\bar{3}c$). Its structure allows for complete solid solution of $Fe^{2+}$ with $Mg^{2+}$ and

$Mn^{2+}$; only limited substitution of $Ca^{2+}$ for $Fe^{2+}$ is possible. The room-temperature-volume specific susceptibility of siderite ranges from 1.3 to 11 $\times$ $10^{-3}$ SI (Hunt et al., 1995) with typical values quoted as 3.8–4.2 $\times$ $10^{-3}$ SI (Rochette et al., 1992) which is distinctly higher than typical paramagnetic minerals (silicates and carbonates). Therefore, siderite-bearing sediments often have a rather high susceptibility (e.g., Mørk et al., 2002). The anisotropy of susceptibility (AMS) in siderites is of the inverse type with the maximum susceptibility axis ($K_1$) corresponding to the crystallographic c-axis. The anisotropy degree P ($P = K_1/K_3$ with $K_3$ being the minimum susceptibility axis) for natural siderite crystals can be as high as 4.7 (Jacobs, 1963). Inverse magnetic fabric (with $K_1$ parallel to the bedding pole rather than $K_3$) observed in limestones is typically attributed to siderite (e.g., Rochette, 1988; Rochette et al., 1992).

Below its Néel temperature, the siderite is antiferromagnetic. It shows a metamagnetic transition at 4.2 K in fields from 10 up to 20 T in agreement with theoretical considerations for highly anisotropic uniaxial antiferromagnets (Jacobs, 1963). The unusually broad transition interval was explained by Dudko et al. (1975): it would be due to multiple sublattices that flip their magnetization one after the other. Eremenko et al. (1985) proposed a magnetic phase diagram for siderite that focuses on high fields at temperatures below 4 K.

Field-cooled (FC) remanences are substantially higher than zero-field-cooled (ZFC) remanences: Frederichs et al. (2003) report for siderite ~8 times stronger FC 5 T isothermal remanent magnetization (IRM) at 2 K. For comparison, the FC 5 T IRM for rhodochrosite ($MnCO_3$) is 40% stronger than the ZFC 5 T IRM. We note here that for both carbonates what is typically referred to as FC IRM is actually a thermoremanent magnetization (TRM) because the samples are cooled through their Néel temperature in a 5 T field. Therefore, from now on we use the acronym TRM@5K for denoting this FC remanence. Large FC/ZFC ratios are considered the most diagnostic property for differentiating between siderite and rhodochrosite (Frederichs et al., 2003). The Néel temperatures of siderite and rhodochrosite differ only by 3 K which makes identification based on that temperature rather equivocal. Because the 5 T FC TRM@5K and ZFC IRM curves differ greatly, Frederichs et al. (2003) argued that siderite is far from magnetic saturation in 5 T fields at 2 K. Because siderite is an antiferromagnet, its remnant magnetic moment is caused by defects and impurities which depend on chemistry and crystallinity.

## 3. Siderite Synthesis, Natural Siderite Samples, and Experimental Protocols

Siderite without ferric iron was synthesized before following the procedure of Jönsson and Sherman (2008) which is based on the procedure described by Wiesli et al. (2004). After precipitation and decantation, the solids were dried inside a glovebox under $N_2$ atmosphere overnight. The next day, the precipitates were transferred in glass flasks inside the glovebox, closed with rubber stoppers, and kept in a sealed $N_2$ filled Al-PP-Al bag until use.

We synthesized siderite (samples 1–8) under slightly varying redox conditions (set by varying perchlorate to ferrous iron ratios in solution, cf. Table 1) to explore the potential dependence of siderite's Néel temperature on the amount of ferric iron in the synthesis. Fine-grained siderite oxidizes to iron(oxy)(hydr)oxide mixtures on laboratory time scales. Therefore, siderite products were dried in the glove box used for synthesis and kept under argon in a refrigerator in air-tight vials until the start of magnetic experiments. To monitor potential effects of oxidation on siderite's magnetic properties (Néel temperature, FC and ZFC remanences and the FC/ZFC ratio) the synthetic siderite samples were measured once again in the MPMS instrument (Magnetic Property Measurement System, an MPMS3 SQUID magnetometer instrument from Quantum Design was used) after 1–2 days standing in air in the MPMS sample holder in a refrigerator. The synthesis and XRD analyses were carried out in the Geolab of the Department of Earth Sciences, while some XRD work was done at the Department of Chemistry (both Utrecht University, Netherlands). The MPMS measurements were performed at the Centre de Physique du Globe of Dourbes (Belgium).

The three crystalline hand specimens, labeled 9, 10, and 11, from the mineral collection of the Department of Earth Sciences (Utrecht University) are rather different in their appearance. The surface of sample 9 is beige-brown-greenish in color while pieces are beige. Sample 10 is dark gray with some black spots. The resulting powders are beige and dark gray respectively. Sample 11 is beige in color. Sample 9 contains minor ankerite, while samples 10 and 11 appear to contain a trace of ankerite (cf. Section 4.1.2).

### 3.1. Synthesis of Siderite

For this study, eight samples in total were synthesized using three slightly different synthesis methods. All syntheses were executed in a glove box under 95%/5% nitrogen/hydrogen atmosphere and with ultra-pure (UHQ)

**Table 1**
*Siderite Synthesis Experiments in the Glove Box: Experiment Type, Amount of Chemicals Used, Ferric Iron Content, and Dominant Synthesis Product*

| Sample, exp. method | $NaHCO_3$ (mol) | $Fe(ClO_4)$ | Volume (mol) | Fe add | Runtime (L) | $Fe^{3+}$ | XRD (mMol/min) |
|---|---|---|---|---|---|---|---|
| 1 chemostat | 0.07 | 0.05 | 1.5 | 0.23 | 4 days | 80.08 | non-cryst |
| 2 chemostat | 0.07 | 0.05 | 1.5 | 1.94 | 4 days | 13.73 | chu |
| 3 chemostat | 0.08 | 0.04 | 0.8 | 0.32 | 3 days | 7.23 | chu |
| 4 chemostat | 0.05 | 0.05 | 1.5 | 1.94 | 2 days | 5.61 | chu |
| 5 chemostat | 0.07 | 0.05 | 1.5 | 1.94 | 2 days | 5.55 | chu |
| 6 SFD | 0.06 | 0.05 | 0.5 | 0.017 | 3 days | 5.12 | sid |
| 7 FD | 0.019 | 0.013 | 0.5 | Inst. | 2 mon | 0.97 | sid/chu |
| 8 FD | 0.012 | 0.012 | 0.5 | Inst. | 3 mon | 2.40 | sid |
| 9 hand specimen | n/a | n/a | n/a | n/a | n/a | 1.67 | sid/ank |
| 10 hand specimen | n/a | n/a | n/a | n/a | n/a | n.d. | sid/tr. ank |
| 11 hand specimen | n/a | n/a | n/a | n/a | n/a | n.d. | sid/tr. ank |

*Note*. SFD = shortened free-drift; FD = free-drift; n/a = not applicable; n.d. = not determined; add = addition (of ferrous iron); Inst. = instantaneous; mon = month; non-cryst = non-crystalline; chu = chukanovite; sid = siderite; ank = ankerite; and tr. = trace. Samples 10 and 11 were added at a later stage to the study; their $Fe^{3+}$ content was not determined.

water purged with argon for at least 1 hour ($N_2$ contained <2 ppm $O_2$ and Ar < 0.5 ppm $O_2$). Sodium bicarbonate and iron(II) perchlorate served as carbonate and iron sources, respectively. Perchlorate is a strong oxidant but a weak ligand (Wiesli et al., 2004). Thus, in principle, the resulting siderite should be very pure since the perchlorate will not be incorporated in the siderite crystal structure. The different synthesis procedures yielded siderite with slightly varying Fe(III) content associated with it as partial oxidation could not be completely prevented (see Section 4.1.2 for more information). All three methods start from the premise that larger crystals result when the precipitation process is slower. The ratio of ferric iron to total iron ($Fe_{tot}$), $Fe^{3+}/Fe_{tot}$, of the synthesis products was determined by a slightly modified ferrozine spectrophotometric method described in Section 3.2.

Sample harvesting was delicate because of its propensity to oxidation. The entire process described next was performed inside the glove box unless indicated otherwise. The samples were harvested by extraction of 50 mL suspension with a syringe while keeping the precipitates in suspension by stirring. Afterward the syringes were connected to a filter holder and the content was pressed through a 0.22 µm glass fiber filter. The remaining synthesis products on the filter were washed two times by pressing 50 mL of oxygen-free UHQ water through the filter holder and a third time with anoxic 96% ethanol to accelerate the drying. The filter with the washed solids was then carefully picked up with a cleaned pair of tweezers and put onto a watch glass. Drying took around 3–4 hr on average. After drying, the material was scraped off the filter onto the watch glass and stored in an airtight vial.

#### 3.1.1. Method 1—Free-Drift Experiment

The most straightforward but also most time-consuming method is based on free-drift experiments as described by Romanek et al. (2009). 100 mL of $2.5 \times 10^{-2}$ M Fe(II) perchlorate was mixed with 500 mL of $2.5 \times 10^{-2}$ M sodium bicarbonate inside the glove box. The flask was sealed to prevent the outgassing of $CO_2$ and the solution was left to stand for 3 months. One sample was collected according to the procedure described above while stirring the suspension after 2 months and another after 3 months to explore whether Ostwald ripening would have any visible effect. Samples 7 and 8 were synthesized according to this method.

#### 3.1.2. Method 2—Chemostat Experiment With Controlled pH

The chemostat had to be placed outside the glove box simply because it was too big. It consists of a 2 L glass beaker that is tightly closed with a lid featuring various closable holes for experiment manipulation and control: stirrer, pH sensor, dissolved oxygen sensor, air flow controller, gas escape (a minute overpressure is maintained), transfer of chemicals to and from the experiment (can be connected to the syringe). Experiments are carried out under controlled atmosphere. After specific timings, the samples were collected with the syringe and processed

further inside the glove box. The pH in the chemostat was controlled by purging the solution with an adjustable Ar-$CO_2$ ratio. At the start of the siderite synthesis, the pH was set at 6.5 to keep the dissolved inorganic carbonate fraction essentially at zero. After ferrous perchlorate addition, the $CO_2$-Ar mixture is replaced by increasingly Ar-richer purging gas, making the pH slowly increase. The controlled increase in carbonate in the system enables control of siderite's precipitation rate.

For synthesis experiments, the reactor was filled with 1.25 L UHQ water and was left overnight while purged with argon at a rate of 400 mL/hr. The next day, 50 mM sodium bicarbonate and 50 mM ferrous perchlorate were weighted and brought into the solution in a glovebox. 200 mL of the bicarbonate solution was transferred via four 50 mL syringes to the reaction vessel where the argon flow had been replaced by a $CO_2$ flow. The bicarbonate solution was pumped into the vessel with a syringe pump. By pumping the bicarbonate into the vessel, the pH rose from 4 to 6.5 but then slowly dropped to a value between 6.1 and 6.3. Meanwhile, ferrous perchlorate was removed from the reactor using syringes. When the pH was lower than 6.5, it was pumped in the vessel at a rate of 5 mL/min. After 2 hours, the $CO_2$ flow was completely replaced by an argon flow again to raise the pH and therefore induce precipitation. After the pH reached 7.5, the experiment was left to stand overnight.

The next day, the suspension inside the reactor was collected with syringes and transferred as quickly as possible to the glovebox. There, the solids were washed, dried, and stored as described before. Samples 1–5 were synthesized with the chemostat.

#### 3.1.3. Method 3—Shortened Free-Drift Experiment

This experiment type combines elements of methods 1 and 2. Ferrous perchlorate was added to a bicarbonate solution at a very slow rate inside a glovebox. This glove box did not allow usage of $CO_2$ (or any other gas) for pH regulation and the very slow addition is anticipated to cope with the lack of pH control. The purpose is to create a well-crystalline siderite while not having to wait for months.

A syringe pump was transferred into a glovebox and a magnetic stirrer was installed underneath a 0.5 L beaker filled with a 0.12 M bicarbonate solution. A hole was drilled into the lid to fit in a tube which was connected to the syringe. The hole had to be as small as possible to minimize $CO_2$ outgassing. Then, 100 mL of 0.5 M ferrous perchlorate was pumped with 50 mL syringes into the bicarbonate solution at a rate of 2 mL/hr while stirring. After 2 days, all the ferrous perchlorate had been added and the sample was left to age for one more day before it was harvested in the same way as described before. Sample 6 was synthesized in this manner.

### 3.2. Ferrozine Method

Ferrozine ($C_{20}H_{12}N_4Na_2O_6S_2$) forms a stable complex (pink-purple colored) with dissolved ferrous iron with maximum absorbance at 562 nm (Gibbs, 1976; Stookey, 1970). The complexation reaction is $3(C_{20}H_{13}N_4O_6S_2)^- + Fe^{2+} + Na^+ \rightarrow Fe(C_{20}H_{13}N_4NaO_6S_2)_3$. Only ferrous iron can be measured, not ferric iron. The procedure adopted is as follows: the sample is split into two aliquots with one measured as is. The iron in the other aliquot was fully reduced to ferrous iron by hydroxylamine (Viollier et al., 2000). The difference in absorbance serves to calculate the [$Fe^{3+}$] (Viollier et al., 2000). Absorbance was measured using a Shimadzu spectrophotometer. It should be noted that it is undetermined whether the ferric iron is incorporated in the siderite, sorbed, or intergrown as a ferric iron phase.

Chemicals involved are a ferrozine solution containing 10 mM ferrozine and 100 mM ammonium acetate, a reducing agent containing 1.4 M hydroxylamine hydrochloride in 2 M HCl, and a buffer solution containing 5 M ammonium acetate adjusted to a pH 9.2 with ammonium hydroxide. Inside the glove box samples were variably diluted in oxygen-free 0.5 M HCl to keep within the calibrated absorbance limit (0.9).

For all samples (and the calibration series as well) two cuvettes were prepared: one for the $Fe^{2+}$ measurement and one for the total iron ($Fe_{tot}$) determination. 1.5 mL sample suspension was added followed by 200 µL ferrozine solution. 300 µL UHQ and 400 µL buffer solution was added to $Fe^{2+}$ cuvettes and the absorbance was measured after shaking. 300 µL of the reducing agent was added to the $Fe_{tot}$ cuvettes; they were stirred and left standing for 10 min for the reduction to occur. After this operation the 400 µL buffer solution was added; subsequently, samples were measured as described before. With the calibration lines, the ferric/ferrous ratio in the synthesis products could be calculated.

### 3.3. X-Ray Diffraction

X-ray diffractograms were taken with a Bruker D2 Phaser ($CoK_{\alpha}$) for each sample from 10° to 80° 2Θ in steps of 0.02° 2Θ and 1 s counting time per step. The synthetic samples appeared to be very sensitive to oxidation in air. To prevent oxidation artifacts during the measurements, the samples were coated with 99% glycerol. Glycerol (X-ray amorphous) does not interfere with X-ray reflections of the samples and effectively prevents oxidation by air (see Figure S1 in Supporting Information S1). Sample preparation was done inside the glove box. To test the efficacy of glycerol treatment, a subsample of the most reactive sample (sample 3) was measured first while another subsample was measured a few hours later. Natural siderites were analyzed with a Bruker AXS D8 instrument equipped with a Lynxeye XE-T detector between 3° and 73° 2Θ with a 0.02° 2Θ step size and 0.85 s counting time per step ($CuK_{\alpha}$ radiation); powdering was done under ethanol with a mortar and pestle to minimize oxidation. The unit cells of the siderites were calculated using Rietveld refinement (see Supporting Information S1).

### 3.4. MPMS Measurement Sequence

All measurements were done with a MPMS3 (magnetic property measurement system) instrument from Quantum Design (San Diego, CA, USA) equipped with the Evercool system. Samples were weighed with an Ohaus semi-microbalance. Before the measurements, the MPMS3 was calibrated using the Pd standard reference sample provided by Quantum Design following the manufacturer's routine calibration procedure for the magnetic moment calibration. The instrument sensitivity is $2.4 \times 10^{-12}$ $Am^2$; the magnetic moments of all samples were at least two orders of magnitude higher. The MPMS brass holder was always used. Powder samples were loaded in Quantum Design powder capsules made of low-temperature-resistant plastic.

Synthesis samples 2–5 tarnish quickly (within minutes); therefore, all powders were kept in the sealed vials filled with Ar until the very latest moment possible. The time from vial opening until installation in the MPMS was typically about 70 s. Once inside the MPMS, the sample chamber was purged with He and kept under a pressure of ∼1 kPa. Siderites from the mineral collection were gently ground under absolute ethanol with a mortar and pestle, and left to dry before weighing and mounting in the MPMS. Those samples did not tarnish.

Magnetic moment versus temperature measurements were performed to detect the Néel temperature of siderite as well as ordering temperatures and/or magnetic transitions of potentially present other magnetic phases. The instrument was programmed to be in "ramp-mode" during either temperature-dependent or field-dependent measurements. A cooling or warming cycle between 300 and 5 K typically lasts ∼1 hr with ∼1,750 data points collected. Measuring a hysteresis branch from +5 to −5 T takes ∼80 min (∼300 data points). Samples were subjected to the following measurement sequence with weak applied fields first to minimize potential magnetic history effects:

1. Measure the magnetic moment during cooling from 300 to 5 K in a weak field of 15 mT, referred to as the WFC curve (weak-field-cooled). Below its Néel temperature, siderite is a very hard antiferromagnet (i.e., far from magnetic saturation in a 5 T field at 2 K, e.g., Frederichs et al., 2003). Therefore, cooling in a 15 mT field (which is much smaller than the coercive force of siderite) is expected to produce a Hopkinson peak just below the Néel temperature. The observation of a Hopkinson peak would facilitate the detection of siderite at low concentrations.
2. Magnetize the sample in a 5 T field at 5 K. The field is switched off at 5 K, obtaining an IRM at 5 K (IRM@5K). Thereafter, the IRM@5K is warmed in zero fields to 300 K. This warming curve is referred to as zero-field-cooled (ZFC) warming curve (the 15 mT is considered to have induced solely reversible magnetic behavior in siderite below its Néel temperature, a plausible assumption given the presence of a Hopkinson peak).
3. Measure the magnetic moment in a 5 T field during cooling from 300 to 5 K. This measurement is referred to as strong-field-cooled (SFC) curve. A Hopkinson peak is probably not visible given the anticipated appreciable magnetization contribution to the curve.
4. The field is switched off at 5 K and the field-cooled (FC) TRM@5K (TRM at 5 K) is warmed to 300 K, referred to as the FC warming curve. Because more grains are blocked during the SFC (it is a TRM induced in a 5 T field), the FC warming curve is expected to lie above the ZFC warming. This has been verified for example, by Frederichs et al. (2003).

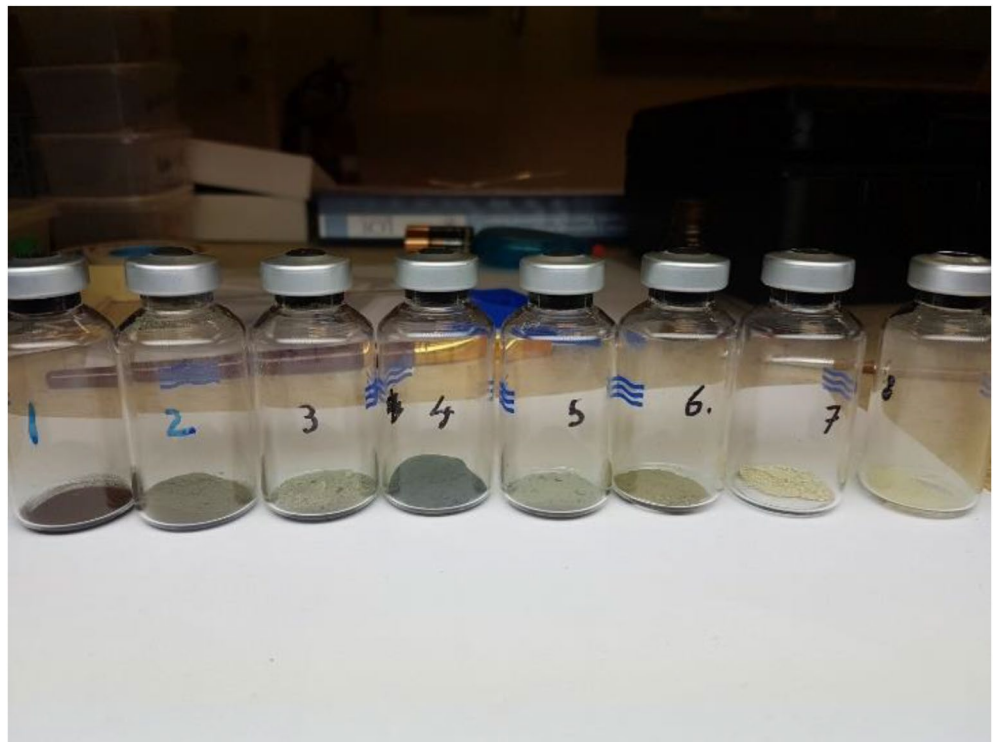


**Figure 1.** Vials with synthesis products.

5. Measurement of a hysteresis branch at 300 K. A hysteresis branch involves the measurement of the magnetic moment from a +5T field to a −5 T field. A paramagnetic-like linear curve through the origin is expected above the Néel temperature of the siderite. It serves as a check for a permanent magnetic moment at room temperature that potentially may have been caused by the siderite tarnishing.
6. Demagnetizing the sample at 300 K using the MPMS protocol followed by cooling to 5 K in zero fields and measurement of a hysteresis branch at 5 K. For some samples, the hysteresis branch was also measured at 5 K after cooling from 300 K in a field of 5 T. Possible exchange bias (shifting of the branch with respect to the origin) can then be detected by the ZFC and FC hysteresis branches (see Table S2 for the small data set available). The branches should "open" as siderite is below its Néel temperature. The measured hysteresis branches are likely part of a minor hysteresis loop since a 5 T field does not saturate siderite, as seen from the large difference between the ZFC and FC warming curves.

Samples 1, 4, and 6–10 were subjected to the MPMS measurements described above. To study the effects of siderite oxidation, samples 6–8—the slowly tarnishing synthetic siderites—were subjected again to this procedure after 1–2 days storage in a refrigerator in air (in the MPMS powder capsules). The Néel temperature was determined by the two-tangent method (Grommé et al., 1969).

## 4. Results

### 4.1. Description of the Synthesis Products

#### 4.1.1. Color

Samples 1–5 were synthesized with the chemostat. Upon addition of the ferrous perchlorate, the transparent solution turned immediately rusty-orange. The lack of a visible precipitate likely indicates that ferric iron colloids were responsible for the coloring. During and after the pH increase, variably colored blueish precipitates started to develop overnight. After completing the synthesis process, suspensions were transferred to the glove box for drying and their color did not change during this operation. The synthesized powders are shown in Figure 1. Samples 2–5 are blueish gray (Munsell codes 2 = 5PB6/6, 3 = 5PB7/6, 4 = 5PB3/6, and 5 = 5PB8/4), with sample 1 being more brown-black (2.5YR1/2). Sample 1 unfortunately dried under slightly oxygenated

conditions (incidentally some air slipped in the glove box); during drying, its color changed from blueish gray to dark brown indicating oxidation. The ferrozine method yielded a high percentage of ferric iron (Table 1), while the XRD diffractogram pointed to an essentially non-crystalline product. When testing the transfer of the samples to storage vials held in air, the test batches changed color from blueish gray to black within seconds. Therefore, the samples were put into air-tight storage vials inside the glove box and kept under argon up to the magnetic experiments.

Samples 6–8 were synthesized with the (shortened) free drift method. In sample 6 (shortened free drift), a beige precipitate started to form after ~30 min. The color remained stable during the 3 days of the experiment. During drying in the glove box, the beige color became slightly more intense. In the case of sample 7 (free drift), a beige-white precipitate started to form several minutes after mixing the reaction solutions. In the case of sample 8 (free drift), the precipitate was slightly lighter in color than in sample 7. The color of the samples produced with both experiments did not display further changes in time. The precipitates accumulated on the bottom of the reaction vessel, but light stirring easily brought the precipitates back into the suspension. With time, the "stirring force" required for resuspension slightly increased, hinting at growing particles. Samples 7 and 8 were collected after two and 3 months respectively. The samples became slightly beige in color during drying in the glove box. The color of samples 6–8 is distinctly beige than that of samples 2–5 (Figure 1; 6 = 10YR5/2, 7 = 10YR9/2, and 8 = 10YR9/2). While testing transfer to vials in air, samples 6–8 tarnished as well but much slower than samples 2–5. A marked color change occurred after a few hours only. Nonetheless, samples 6–8 were also stored and kept under argon until the magnetic experiments, like samples 1–5.

#### 4.1.2. XRD Characterization

Small portions of the synthesis products were prepared for XRD analysis inside the glove box, that is, the coating or mixing with glycerol was done inside the glove box. Two XRD samples were made from the reactive sample 3: one was measured first (sample 3b) in the series of XRD runs while the other glycerol-coated sample was kept in air and measured after 5 hr (sample 3a). Clearly, the peak height decreased while the width increased in sample 3a compared to 3b, testifying the effects of oxidation (Figure S1 in Supporting Information S1).

The X-ray diffractograms of the synthesis products (Figure 2) confirm observations pertaining to color and proneness to oxidation: samples 2–5 are distinctly less crystalline than samples 6–8 (sample 1 is largely oxidized to essentially non-crystalline material). The major peaks in samples 2–5 correspond to chukanovite ($Fe_2(CO_3)(OH)_2$) while samples 6 and 8 indicate siderite and sample 7 represents a mixture of siderite and chukanovite. These are the only phases detected by XRD. The presence of X-ray amorphous sorbed or intergrown phases cannot be excluded. Such phases may contain (most of) the ferric iron measured (see Section 4.1.3). However, as will appear later the synthetic siderite's proneness to tarnishing and their measured magnetic behavior shows a relation to the total ferric iron content of the synthesis products. "Siderite Alejandra" is a natural siderite used by Morera-Chavarría et al. (2016). Samples ("standards") 9, 10, and 11 are siderites from the mineral collection of the Department of Earth Sciences. XRD shows that they are much more crystalline than the synthesis products; sample 9 appears to contain minor ankerite ($(Mg,Fe)Ca(CO_3)_2$) and samples 10 and 11 contain trace amounts of ankerite. The siderites appeared to be of high purity as shown by total reflection X-ray fluorescence data (Text S2 in Supporting Information S1): some Mn substitution was measured (with the measured Ca assumed to be allocated to ankerite). The unit cells (from Rietveld refinement, see Supporting Information S1) are very similar to the reference values for siderite.

Chukanovite as the only detectable mineral in samples 2–5 is unexpected. While the compound was known before as a steel corrosion product, chukanovite has only recently been described as a mineral (Pekov et al., 2007); it is a fine-grained colorless to light green acicular mineral with brownish-green surfaces in aggregates. It is a carbonate-bearing oxidation product of metallic iron occurring in meteorites and structurally related to malachite. It is not stable under ambient conditions. Intergrowths with siderites occur (Pekov et al., 2007). Presumably the pH (set at 7.5) was too high during the siderite aging: with the surplus $OH^-$ available and sufficient $CO_3^{2-}$, chukanovite may have been formed rather than the anticipated siderite.

#### 4.1.3. Ferric Iron Content

The ferric iron content in the synthesis products does not appear to vary substantially (Table 1). Siderite and chukanovite are nominally ferrous iron phases; their ferric iron content should be low. Thus, as noted before, ferric iron may be associated with sorbed or ferric iron phases intergrown with siderite or chukanovite. The black

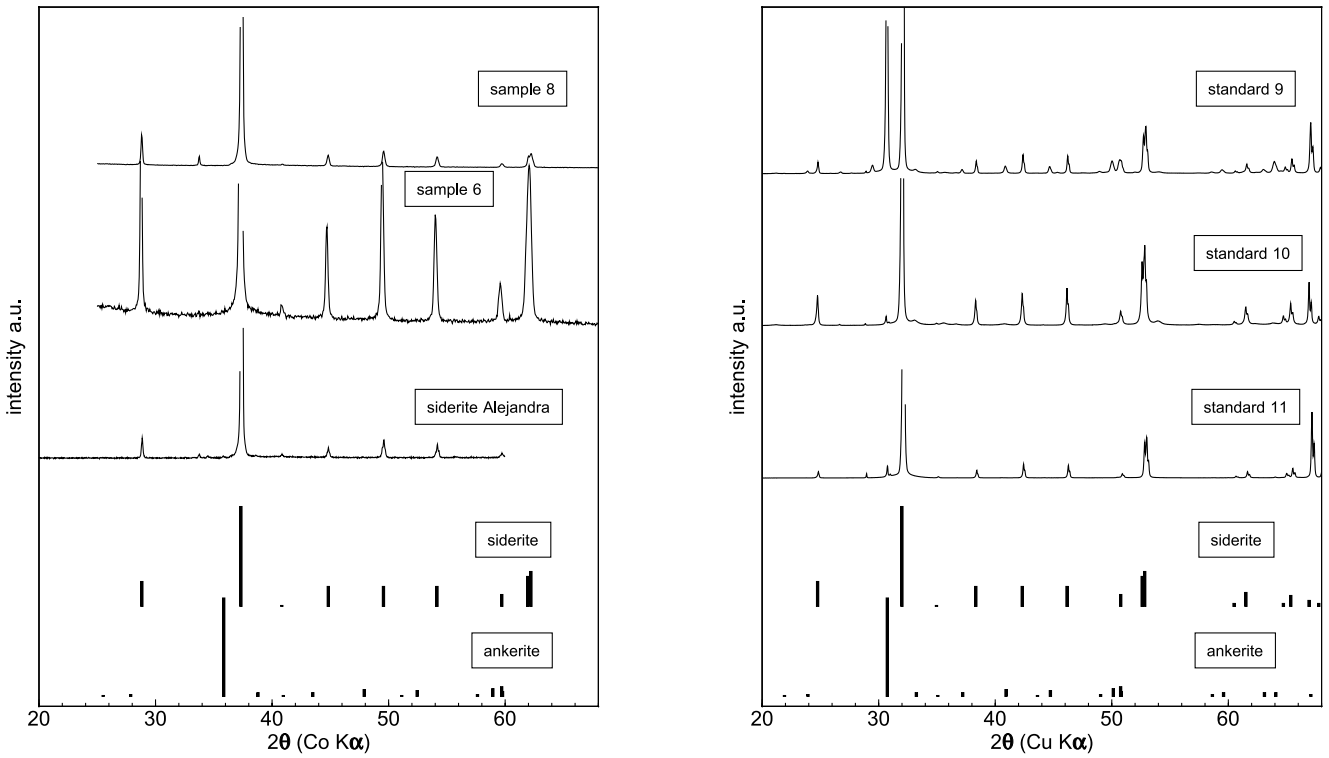


**Figure 2.** X-ray diffractograms of the synthesis products and hand specimens. The diffractograms were normalized to the maximum intensity and presented in the same relative scale but with the highest peak truncated in order to enhance the visibility of the diffractions with smaller intensities. The strongest peaks of the X-ray powder pattern are given below for each reflection as [d(Å), I, (hkl)]. Siderite strongest reflections (Graf, 1961): 3.59, 35, (012); 2.791, 100, (104); 2.344, 20, (110); 1.963, 20, (202); 1.737, 20, (018); and 1.730, 30, (116). Space group: hexagonal $R\bar{3}C$. Chukanovite strongest reflections (Pekov et al., 2007): 6.14, 40, (200); 5.15, 60, (231); 3.73, 80, (310); 2.645, 100, (230); 2.361, 40, (510); and 2.171, 40, (520). Space group: monoclinic $P2_1/a$.

non-crystalline sample 1 is largely oxidized. Typical ferric iron contents of the other samples straddle around 5% with chukanovite samples containing somewhat more ferric iron than siderite samples. The free-drift experiments have the lowest ferric iron content. Apparently, slow synthesis leads to the purest siderites. Note that sample 7 contains siderite and chukanovite. The ferric iron contents appeared to be in line with the propensity to change color upon exposure to air; the fastest changing samples have the most ferric iron. Hand specimen 9 has 1.7% ferric iron.

### 4.2. Rock Magnetic Results

Next to the hand specimens, samples 6–8 are thus most insightful to investigate siderite's magnetism. Samples 6 and 8 contain siderite only, while sample 7 is a mixture of siderite and chukanovite. As expected, the hand specimen samples 9 and 10 display the classical siderite behavior (Figure 3, Table 2). For completeness, the behavior of samples 1 (largely oxidized) and 4 (chukanovite) is shown in the Figure S2 in Supporting Information S1.

#### 4.2.1. Natural Siderites

Samples 9 and 10 were subjected to the MPMS measurement sequence described above; hysteresis branches at 5 and 300 K were measured for samples 6 and 8 as well (Figures S4 and S5, Table S1 in Supporting Information S1). Sample 11 was used to measure the hysteresis loops at 5 and 300 K. As expected, a pure paramagnetic signal was determined at 300 K. At 5 K, the loops barely open, indicating a hard antiferromagnetic structure. Data are included in Table S2 and Data Set S4.

SFC curves show their maximum at the Néel temperature (Figure 3a); the maxima form a 1.5–2 K wide plateau. Sample 9 has a Néel temperature of 37 K typical of siderite. The Néel temperature of sample 10 of 40–41 K is higher than expected for pure siderite. The increase in magnetic moment in sample 9 below 13 K is inferred to be due to the minor ankerite present that magnetically orders below 1.7 K (Hilscher et al., 2005). The WFC curves

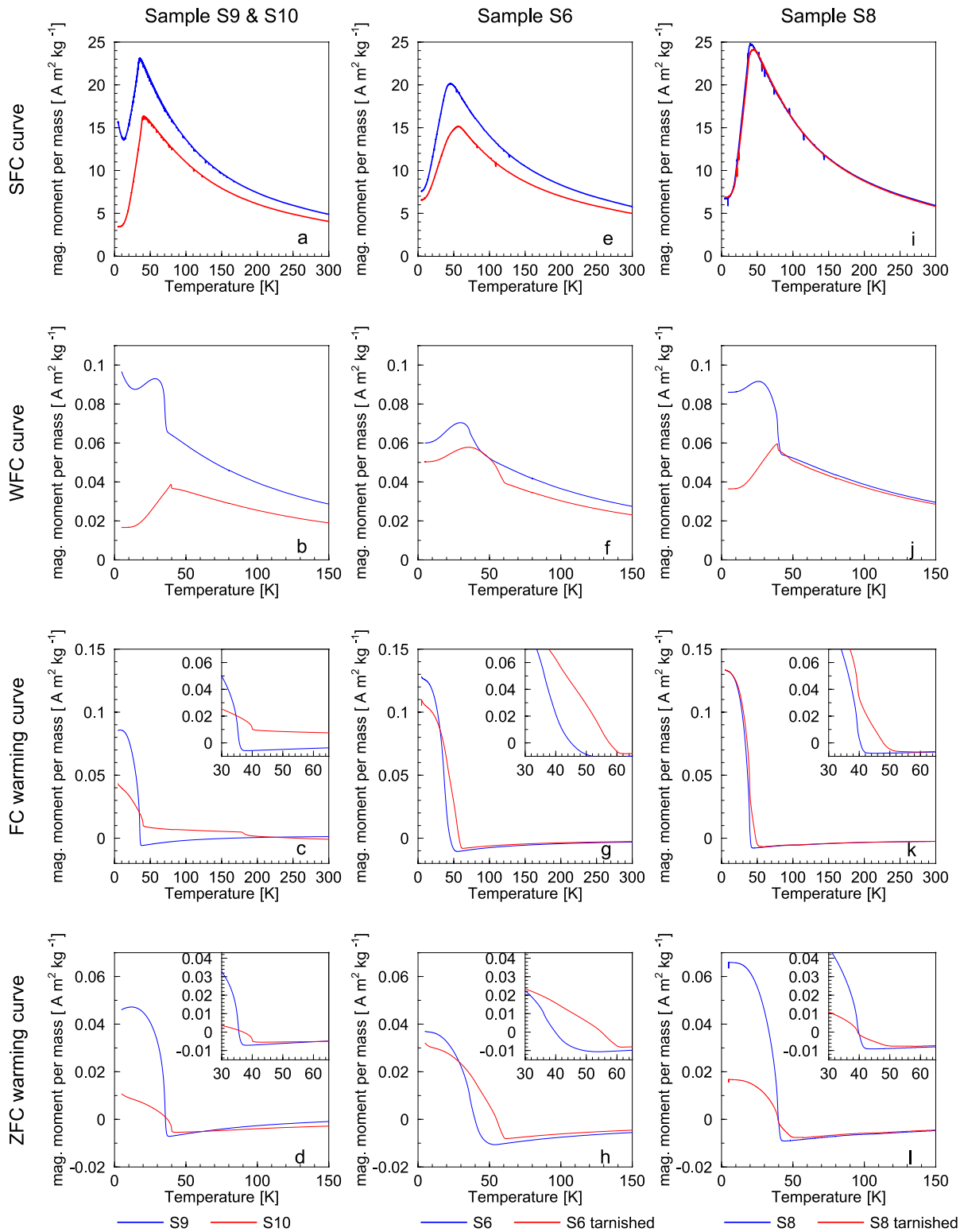


**Figure 3.** Low-temperature data of the siderite samples, left column (a–d): natural samples 9 (S9, blue curves) and 10 (S10, red curves); central column (e–h): synthetic sample 6 (S6, blue curves: measured immediately after opening of the vial; red curves: sample measured again after 2 days storage in air in a refrigerator); right column (i–l): synthetic sample 8 (S8, blue curves: measured immediately after opening of the vial; red curves: sample measured again after 2 days storage in air in a refrigerator). (a, e, and i) Cooling curves in a 5 T field. (b, f, and j) Weak field cooling curves: cooling in a 15 mT field. (c, g, and k) Warming curves of field-cooled (5 T field) 5 T isothermal remanent magnetization (IRM) at 5 K. (d, h, and l) Warming curves of a "zero-field" cooled (15 mT field) 5 T IRM at 5 K.

**Table 2**
*Magnetic Properties of the Siderites Sample*

| Sample | ZFC mom. at 5K ($Am^2/kg$) | FC mom. at 5K ($Am^2/kg$) | FC/ZFC | Neel temp (K) | | | Warm. $ZFC_{lo}$ | Warm. $ZFC_{up}$ | Warm. $FC_{lo}$ | Warm. $FC_{up}$ |
|---|---|---|---|---|---|---|---|---|---|---|
| | | | | | Hop | | | | | |
| | | | | FC | lo | up | | | | |
| 6 | 0.037 | 0.128 | 3.46 | 45.0 | 37.2 | 43.6 | 36.4 | 51.0 | 36.0 | 52.0 |
| 6 ox. | 0.031 | 0.109 | 3.42 | 56.0 | n/a | 60.4 | n/a | 60.6 | n/a | 60.6 |
| 7 | 0.045 | 0.264 | 5.81 | 40.2 | 39.7 | n/a | 39.7 | n/a | 39.7 | n/a |
| 7 ox. | 0.093 | 0.299 | 3.22 | 42.3 | 39.8 | n/a | 39.8 | n/a | 39.9 | n/a |
| 8 | 0.066 | 0.133 | 2.02 | 40.6 | 39.6 | 41.3 | 39.6 | 41.1 | 39.6 | 41.3 |
| 8 ox | 0.017 | 0.133 | 7.94 | 44.5 | 39.6 | 40.1 | 40.0 | 48.6 | 40.0 | 49.1 |
| 9 | 0.046 | 0.085 | 1.86 | 36.0 | 36.7 | n/a | 37.2 | n/a | 36.9 | n/a |
| 10 | 0.011 | 0.043 | 4.06 | 41.1 | 40.2 | n/a | 40.2 | 41.1 | 40.2 | n/a |
| F | 0.051 | 0.381 | 7.43 | 36.7 | n.d. | n.d. | 37 | | 37 | |
| A | 0.010 | 0.064 | 6.18 | 38.2 | 38.4 | n/a | 38.8 | n/a | 38.6 | n/a |

*Note*. ZFC = zero-field cooled (cooling in a 15 mT field is equivalent to zero-field cooled); FC = field cooled (in 5 T field); mom. = magnetic moment per unit mass; Temp = temperature; Néel temperature FC: determined from the maximum during cooling in a 5 T field; Hop = Hopkinson peak, Néel temperature determined from: lo = lower temperature of the Hopkinson peak, up = upper temperature of that peak; warm. = Néel temperature determined from warming curve of the respective cooling treatment in the MPMS, $ZFC_{lo}$ = lower temperature of the "Néel temperature tail," $ZFC_{up}$ = upper temperature of that tail (both for zero/weak-field cooled remanences); and $FC_{lo}$ and $FC_{up}$: same as for ZFC but not for field-cooled remanences. Formula Frederichs' siderite (F) under assumption only carbonate and no oxidation: $(Fe_{0.81}Mn_{0.06}Mg_{0.12}Ca_{0.01})(CO_3)$ (Frederichs et al., 2003). A = siderite of Morera-Chavarría et al. (2016). The corresponding magnetic behavior is shown in Figure S3 in Supporting Information S1.

show a variable expression of a Hopkinson peak: in sample 9 it is prominently present while in sample 10 it is barely visible (Figure 3b); as anticipated, Néel temperatures derived from the Hopkinson peak correspond to those from the FC curves: ~36.5 and ~40 K respectively. The 5 T FC remanence at 5 K in sample 9 (0.085 $Am^2/kg$) is about twice that of sample 10 (0.043 $Am^2/kg$; cf. Table 2, Figure 3c). The FC/ZFC ratio varies as expected for antiferromagnetic minerals: it is 1.86 for sample 9 (ZFC 5 T IRM at 5 K: 0.046 $Am^2/kg$) and 4.06 for sample 10 (ZFC 5 T IRM at 5 K: 0.011 $Am^2/kg$; Table 2, Figure 3d). The FC and ZFC warming curves of sample 10 decay steadily toward the Néel temperature, while those of sample 9 show a plateau-like behavior (FC) or even a minor increase (ZFC) (Figures 3c and 3d) on warming up to ~20 K. The FC warming curve of sample 10 shows a marked first derivative discontinuity at 180 K (Figure 3c) which is absent in its ZFC warming curve. This is unexpected, since only siderite with a trace of ankerite is detected by XRD (cf. Figure 2 left panel). The same feature is not detected in the other samples. We can only speculate on a possible explanation for it. This discontinuity is detected in the SFC curve and not in the 5T IRM@5K ZFC warming curve, which means that the source is activated only upon cooling in a strong field.

#### 4.2.2. Synthetic Siderites With Variable Associated Ferric Iron Content

Synthetic siderites with associated ferric iron show magnetically typical siderite behavior during low-temperature measurements, at least when fresh sample material is considered. Samples 6 (5.1% $Fe^{3+}$, Figures 3e–3h) and 8 (2.4% $Fe^{3+}$, Figures 3i–3l) are shown here; data of sample 7 (1.0% $Fe^{3+}$, a mixture of siderite and chukanovite) is placed in Supporting Information S1. The SFC curves show their maximum around the expected temperature range; its expression is broader than that of the well crystalline natural siderites (Figures 3a, 3e, and 3i). The maximum temperature seems to increase with $Fe^{3+}$ content: 40.2 K in sample 7, 40.6 K in sample 8, and 45 K in sample 6 (Table 2). The Hopkinson peak is broader (Figures 3f and 3j) than in the natural siderites (when present, Figure 3b); tarnishing shifts its expression to higher temperatures (sample 6, Figure 3f) but it can also become very subdued (sample 8, Figure 3j). The 5 T TRM@5K FC and ZFC warming curves show the expected decay when warming from 5 K through the Néel temperature; however, both curves display remanence tails at higher temperatures. Such tails are absent in the crystalline natural samples. The tailing behavior is dramatically amplified by tarnishing and seems to be a function of $Fe^{3+}$ content. For sample 7 (1.0% $Fe^{3+}$) in the Néel

temperature does not change noticeably upon tarnishing (Supporting Information S1) and is comprised between 39.7 and 39.9 K (Table 2). However, fresh sample 8 (2.4% $Fe^{3+}$) shows a tail between ~39.5 and ~41 K ($ZFC_{lo}$ vs. $ZFC_{up}$ and $FC_{lo}$ vs. $FC_{up}$ in Table 2), which widens to ~40–49 K after 1–2 days of tarnishing (Figures 3k and 3l, Table 2). Fresh sample 6 (5.1% $Fe^{3+}$) has a tail between ~36 and ~52 K. Tarnished sample 6 shows no tail anymore while the FC and ZFC curves are shifted to an ordering temperature of 60–61 K (Table 2, Figures 3g and 3h). The mass-specific FC 5 T TRM@5K of the synthetic siderites (0.10–0.25 $Am^2/kg$) is higher than that of the natural siderites (0.04–0.08 $Am^2/kg$), cf. Table 2. 5T ZFC IRM@5K values of the synthesized siderites (~0.035–0.065 $Am^2/kg$) are more akin to natural siderite (~0.04–0.05 $Am^2/kg$). Upon tarnishing the specific 5 T TRM@5K lowers, this effect is most pronounced in the ZFC 5 T IRM@5K (Table 2, Figures 3d, 3h, and 3l).

The hysteresis loops measured at 300 K are paramagnetic; possibly present impurities are too small to express magnetization at room temperature. Hysteresis loops at 5 K are far from saturation, indicating that siderite is a hard antiferromagnet (Figures S4, S5 in Supporting Information S1, Table S2). Below the Néel temperature, the FC loops are offset: the vertical offset coincides with the SFC moment and is therefore caused by the strong-field moment imparted during cooling in the 5 T field. Loops after field cooling in 5 T were measured for sample 9, where the exchange bias field at 5 K is ~−18 mT (Table S2). Loops measured after ZFC have a much smaller offset. Parameters derived from the hysteresis measurements are compiled in Table S2.

## 5. Discussion

The measured magnetic properties of the incipiently altered siderites appear to be appreciably variable. Concentration-independent parameters are most useful for detecting the presence of siderite in natural samples. These include the ratio of the FC 5 T TRM@5K FC and the ZFC 5 T IRM@5K (FC/ZFC in Table 2) and the Néel temperature. The FC/ZFC ratio varies between ~1.9 and ~6.8 (Table 2) without systematic differences between natural and synthetic samples with various degrees of tarnishing. The siderite described in Frederichs et al. (2003) has an FC/ZFC value of ~7.4. FC/ZFC of rhodochrosite ($MnCO_3$) and vivianite ($Fe_3(PO_4)_2.8H_2O$) are ~1.4 and ~1.2 respectively (Frederichs et al., 2003). Thus, higher FC/ZFC values can be considered diagnostic for siderite. Conservatively, we set the lower FC/ZFC "cut-off" at 3. However, the lower "cut-off" of a FC/ZFC diagnostic for siderite is only broadly defined because the FC/ZFC values for other authigenic carbonates and phosphates are poorly known.

The Néel temperature of well crystalline siderite is 37 K and that of rhodochrosite 34 K, while vivianite shows a two-stage magnetic ordering below 12 K (Frederichs et al., 2003). Magnetic transitions in some pyrrhotite polytypes occur also in the 30–35 K range, whereas potential confusion of siderite for other magnetic sulfides, that is, greigite ($Fe_3S_4$) or smythite ($Fe_9S_{11}$) is also possible (e.g., Horng, 2018; Horng & Roberts, 2018; Horng et al., 2020; Rochette et al., 1990). This complicates the attribution of a discontinuity at 36–38 K in (Z)FC warming curves to siderite, as illustrated in Housen et al. (1996). Siderite is metastable at ambient conditions and fine grained siderite oxidizes (or tarnishes) at a laboratory time scale, particularly when ferric iron impurities or sorbed ferric iron is present, as shown by the synthetic samples. The temperatures of the maxima in 5 T cooling curves of the synthetic samples increase with the amount of ferric iron in the synthesis products and with tarnishing (Table 2). Tarnishing appears to smear out the Néel temperature in the IRM@5K ZFC and FC warming curves; it produces a remanence tail up to ~50 K depending on the amount of ferric iron present. The most extreme case (sample 6 tarnished) is characterized by smooth warming curves with a single Néel(?) temperature of ~60 K, which would never be attributed to siderite or an oxidation product of it without pre-knowledge of the sample material. The FC curve maximum at 56 K might indicate that this sample has been transformed into another phase. Ferrihydrite comes in several varieties (2-, 4-, and 6-line ferrihydrite, e.g., Childs (1992)) with reported blocking temperatures between 60 and 120 K (e.g., Guyodo et al., 2006; Zergenyi et al., 2000). The presence of room temperature remanence in ferrihydrite (Berquó et al., 2007) is associated with ferrihydrite formation at temperatures above 130°C and is related to Si-substituted ferrihydrite (Berquó et al., 2007). However, we refrain from speculating about the presence of ferrihydrite because we could not check the material with XRD. Also, the hysteresis loops at 5 K do not show signs of saturation (see Figures S4 and S5 in Supporting Information S1). Note that the largely oxidized sample 1 (with chukanovite as original material) shows a drastically different magnetic behavior (see Figure S2 in Supporting Information S1), so oxidation starting from chukanovite or siderite may yield different products.

Ferric iron present in impurities in the siderite or sorbed on its surface induces a magnetization tail beyond the nominal Néel temperature by a few Kelvin to above 40 K. The substitution seems to be minor in the natural sample 10 with a Néel temperature of 41 K (albeit that Mg cannot be measured with total reflection X-ray fluorescence, see Text S2 in Supporting Information S1). However, since no chemical analysis of ferrous and ferric iron is available for this sample, all remain rather speculative at this stage. Nevertheless, tails of up to 45–50 K can be associated with partially oxidized siderite. Ongoing oxidation might be traceable through enhanced tails whose development can be followed by repeated MPMS measurement. Therefore, in the detection of siderite "Néel" temperatures slightly above 40 K should not be dismissed a priori.

Observation of remanence tails in FC or ZFC warming curves, starting at 35–38 K and extending to 45–52 K, is likely a feature of incipiently oxidized siderite. If one were unaware of this option, these tails could be erroneously associated with phases with a higher magnetic ordering temperature. The potential presence of ilmenite ($FeTiO_3$) with an ordering temperature of 56 K (e.g., Senftle et al., 1975) should not be excluded when interpreting ordering temperatures above 50 K. Siderite oxidation could lead to the formation of ferric iron (hydr) oxides starting at the surface of particles. The ordering temperature of ferrihydrite is dependent on its particle size: Guyodo et al. (2006) report blocking temperatures of 45, 55, or 80 K for 6-line ferrihydrite depending on the synthesis route, arguing that the theoretical Néel temperature for sufficiently large grains would be (relatively far) above room temperature. Zergenyi et al. (2000) reported 85–95 K, so presumably their ferrihydrite has slightly larger grains than those reported by Guyodo et al. (2006). Speculatively, one could relate the enhanced tailing to progressive oxidation starting from the edges of siderite particles, possibly resulting in larger ferrihydrite-like particles with time. This would manifest itself by higher Néel temperatures. However, a definitive answer awaits further work. Exchange bias fields at 5 K from field cooled experiments are negative (Table S2). Lepidocrocite shows concave-down FC and ZFC warming curves without clear discontinuities; however, susceptibility versus temperature curves show a maximum at 52 K interpreted as the Néel temperature (Hirt et al., 2002).

Greigite (e.g., Roberts et al., 2011), pyrrhotite (e.g., Aubourg et al., 2012), and smythite (Horng et al., 2020) may form under similar conditions as siderite and thus should not be excluded beforehand in the "identification decision tree" of siderite. 4C (or 4 M) and 3C (or 3 T) pyrrhotite (Horng, 2018; Horng & Roberts, 2018; Rochette et al., 1990) show a low temperature transition in the temperature range of interest. As already cautioned by Housen et al. (1996), cursory examination of warming curves may lead to erroneous identification of pyrrhotite; FC/ZFC determinations are helpful to robustly determine siderite. Kars et al. (2011) also used a more elaborate low-temperature measurement scheme involving measurement of room-temperature IRM in a small applied field of 5 μT down to 5 K next to classical ZFC warming curves to reinterpret a previous pyrrhotite interpretation (Aubourg & Pozzi, 2010) as siderite.

Next to siderite identification, its quantification is relevant for iron budget calculations. Here, we test the sensitivity of the "magnetic toolkit" with a so-called standard addition experiment. Residual fields in the MPMS instrument might affect the interpretation of warming curves of remanent magnetization: a residual instrument field may yield a large induced magnetization of the sediment matrix in which the siderite is dispersed. Thus, the matrix is relevant. We performed experiments with variable amounts of siderite (siderite sample A) in a calcite matrix (diamagnetic) and a bentonite matrix (paramagnetic). The Hopkinson peak clearly shows up in the diamagnetic matrix irrespective of siderite concentration, whereas its expression is very subdued for low siderite concentrations in a paramagnetic matrix. This complicates siderite quantification in natural samples. The differences between a diamagnetic and paramagnetic matrix are less relevant in the case of FC warming curves (Figures 4a and 4b). A paramagnetic matrix, which is common in natural samples, produces an upward or downward curvature in the warming curves depending on the sign of the residual field in the MPMS instrument in comparison to the remnant magnetization direction. This constrains the selection of an optimal temperature range for quantitative analyses of FC warming curves. We establish a calibration line with the so-called standard addition approach based on FC warming curves (Figure 4c). The approach involves finding an optimal tradeoff between the biggest magnetic moment difference possible below and above the siderite Néel temperature, that is, a temperature interval as wide as possible, and a minimal influence of a residual field in the instrument (potentially varying between subsequent runs), that is, a temperature interval as small as possible. In a diamagnetic matrix, the FC warming curves in the residual field of the instrument include the moments of the TRM@5K (temperature dependent), the induced magnetic moment of the siderite (temperature dependent) and the diamagnetic matrix offset that is independent of temperature. The induced magnetic moment of the siderite that scales with the siderite concentration is the reason for the small differences above the Néel temperature among the curves shown

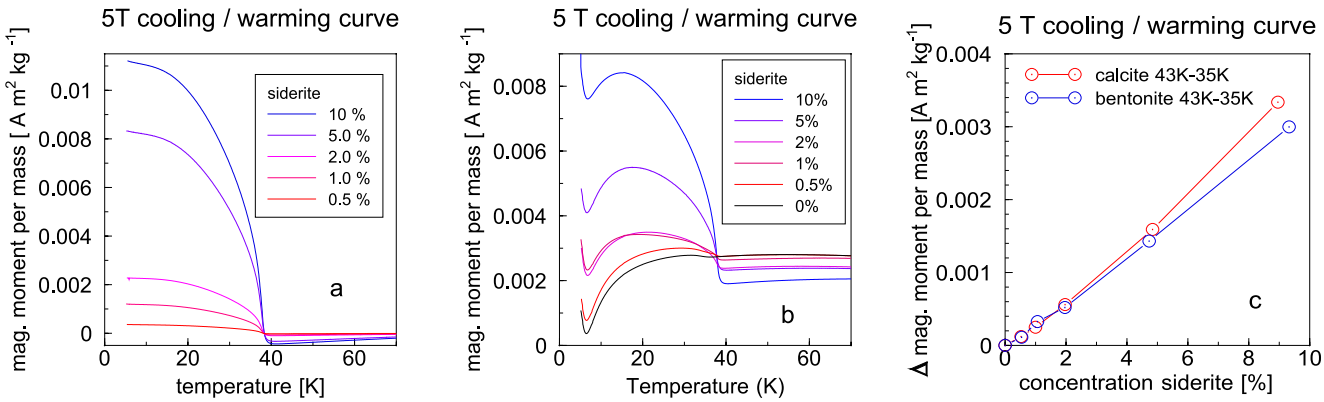


**Figure 4.** Standard addition experiments in (a) a diamagnetic calcite matrix and (b) a paramagnetic bentonite matrix. (c) Corresponding calibration lines.

in Figure 4a. The behavior in a paramagnetic matrix is more complicated: while Curie-Weiss paramagnetism (proportional to 1/(absolute temperature)) in a residual field would result in curling up or down depending on the sign of the residual field, it should be realized that iron-bearing silicates start to magnetically order below ~20 K (this may explain the curling up below ~8 K in Figure 4b). Therefore, focusing on a temperature interval above 30 K is advisable to avoid issues of potential magnetic ordering of matrix minerals. The optimum was reached by considering the 35–43 K temperature range. This evidently includes the Néel temperature, while the impact of a residual field (bound to vary between runs) is marginal because the highest possible temperatures are involved. We acknowledge that simple subtraction of the 35 and 43 K magnetization ignores the temperature dependence of Curie-Weiss paramagnetism of the sediment matrix. Given the fairly large siderite contributions already at low concentrations, we deem this reasonable also seen in the relation to the small temperature interval considered (8 K). As anticipated, the determined calibration lines for a calcite and a bentonite matrix are essentially linear and on top of each other for siderite concentrations below 2% (Figure 4c). The limit of detection limit is estimated at ~0.1% siderite, that is, low-temperature magnetometry is much more sensitive than XRD.

## 6. Conclusions

The presence of ferric iron associated with or sorbed onto fine grained siderite results in a remanence tail beyond the siderite's nominal Néel temperature of ~37 K. Fine grained siderite is metastable under ambient conditions and tarnishing generates a tail in the FC and ZFC warming curves. Field-cooled warming curves have the largest potential for siderite detection in natural samples because they have the most signal and show the largest contrast. FC/ZFC ratios >3 are indicative of siderite. Standard addition indicates a detection limit of 0.1% for low-temperature magnetometry, much lower than more conventional determination approaches.

## Data Availability Statement

All novel magnetic data in the research are included in Supporting Information S1. They are available in the Zenodo repository (Dekkers et al., 2023).

**Acknowledgments**
We gratefully acknowledge the financial support to WH by the Olaf Schuiling Fund for the analyses in this research and Anita van Leeuwen-Tolboom for assistance with the XRD measurements. We thank the Dourbes facility for their hospitality during visits to MJD, WH, and TB. The comments of Ramon Egli and an anonymous reviewer that resulted in a much-improved text are greatly appreciated.

## References

Aubourg, C., & Pozzi, J.-P. (2010). Toward a new<250°C pyrrhotite-magnetite geothermometer for claystones. *Earth and Planetary Science Letters*, *294*(1–2), 47–57. https://doi.org/10.1016/j.epsl.2010.02.045

Aubourg, C., Pozzi, J.-P., & Kars, M. (2012). Burial, claystones remagnetization and some consequences for magnetostratigraphy. *Geological Society, London, Special Publications*, *371*(1), 181–188. https://doi.org/10.1144/sp371.4

Berquó, T. S., Banerjee, S. K., Ford, R. G., Penn, R. L., & Pichler, T. (2007). High crystallinity Si-ferrihydrite: An insight into its Néel temperature and size dependence of magnetic properties. *Journal of Geophysical Research*, *112*(B2), B02102. https://doi.org/10.1029/2006jb004583

Childs, C. W. (1992). Ferrihydrite: A review of structure, properties and occurrence in relation to soils. *Zeitschrift für Pflanzenernährung und Bodenkunde*, *155*(5), 441–448. https://doi.org/10.1002/jpln.19921550515

Claff, S. R., Sullivan, L. A., Burton, E. D., & Bush, R. T. (2010). A sequential extraction procedure for acid sulfate soils: Partitioning of iron. *Geoderma*, *155*(3–4), 224–230. https://doi.org/10.1016/j.geoderma.2009.12.002

Dekkers, M. J., Hanckmann, W., Spassov, S., & Behrends, T. (2023). Low temperature magnetic properties of variably oxidized natural and synthetic siderite Dekkers et al., 2023, G-cubed [Dataset]. Zenodo. https://doi.org/10.5281/zenodo.7781001

Dudko, K. L., Eremenko, V. V., & Fridman, V. M. (1975). Investigation of the transition of $FeCO_3$ from the antiferromagnetic to the paramagnetic state under the influence of a strong magnetic field. *Soviet Physics Journal of Experimental and Theoretical Physics*, *41*, 326–332.

Egger, M., Jilbert, T., Behrends, T., Rivard, C., & Slomp, C. P. (2015). Vivianite is a major sink for phosphorus in methanogenic coastal surface sediments. *Geochimica et Cosmochimica Acta*, *169*, 217–235. https://doi.org/10.1016/j.gca.2015.09.012

Ellwood, B. B., Balsam, W., Burkart, B., Long, G. J., & Buhl, M. L. (1986). Anomalous magnetic properties in rocks containing the mineral siderite: Paleomagnetic implications. *Journal of Geophysical Research*, *91*, 12779–12790.

Eremenko, V. V., Kharchenko, N. F., Belyi, L. I., Gillaud, M., Marshan, A., & Feldman, P. (1985). Magnetic phase diagram for $FeC0_3$, an Ising antiferromagnet with anti-ferromagnetic inter- and intrasublattice exchange coupling. *Soviet Physics Journal of Experimental and Theoretical Physics*, *62*, 988–999.

Fillion, G., & Rochette, P. (1988). The low temperature transition in monoclinic pyrrhotite. *Journal de Physique. Colloques*, *49*(C8), C8-907–C8-908. https://doi.org/10.1051/jphyscol:19888412

Frederichs, T., von Dobeneck, T., Bleil, U., & Dekkers, M. J. (2003). Towards the identification of siderite, rhodochrosite, and vivianite in sediments by their low-temperature magnetic properties. *Physics and Chemistry of the Earth*, *28*(16–19), 669–679. https://doi.org/10.1016/s1474-7065(03)00121-9

Gibbs, C. R. (1976). Characterization and application of ferrozine iron reagent as a ferrous iron indicator. *Analytical Chemistry*, *48*(8), 1197–1201. https://doi.org/10.1021/ac50002a034

Graf, D. L. (1961). Crystallographic tables for the rhombohedral carbonates. *American Mineralogist*, *46*, 1283–1316.

Gromme´, C. S., Wright, T. L., & Peck, D. L. (1969). Magnetic properties and oxidation of iron-titanium oxide minerals in Alae and Makaopuhilava lakes, Hawaii. *Journal of Geophysical Research*, *74*(22), 5277–5294. https://doi.org/10.1029/jb074i022p05277

Guo, H., Stüben, D., & Berner, Z. (2007). Removal of arsenic from aqueous solution by natural siderite and hematite. *Applied Geochemistry*, *22*(5), 1039–1051. https://doi.org/10.1016/j.apgeochem.2007.01.004

Guyodo, Y., Banerjee, S. K., Penn, R. L., Burleson, D., Berquó, T., Seda, T., & Solheid, P. (2006). Magnetic properties of synthetic six-line ferri-hydrite nanoparticles. *Physics of the Earth and Planetary Interiors*, *154*(3–4), 222–233. https://doi.org/10.1016/j.pepi.2005.05.009

Hilscher, G., Rogl, P., Zemann, J., & Ntaflos, T. (2005). Low-temperature magnetic investigation of ankerite. *European Journal of Mineralogy*, *17*(1), 103–106. https://doi.org/10.1127/0935-1221/2005/0017-0103

Hirt, A. M., & Gehring, A. U. (1991). Thermal alteration of the magnetic mineralogy in ferruginous rocks. *Journal of Geophysical Research*, *96*(B6), 9947–9953. https://doi.org/10.1029/91jb00573

Hirt, A. M., Lanci, L., Dobson, J., Weidler, P., & Gehring, A. U. (2002). Low-temperature magnetic properties of lepidocrocite. *Journal of Geophysical Research*, *107*(1), EPM5-1–EPM5-9. art# 2011. https://doi.org/10.1029/2001jb000242

Horng, C.-S. (2018). Unusual magnetic properties of sedimentary pyrrhotite in methane seepage sediments: Comparison with metamorphic pyrrhotite and sedimentary greigite. *Journal of Geophysical Research: Solid Earth*, *123*(6), 4601–4617. https://doi.org/10.1002/2017jb015262

Horng, C.-S., & Roberts, A. P. (2018). The low-temperature Besnus magnetic transition: Signals due to monoclinic and hexagonal pyrrhotite. *Geochemistry, Geophysics, Geosystems*, *19*(9), 3364–3375. https://doi.org/10.1029/2017gc007394

Horng, C.-S., Roberts, A. P., Chen, Y.-H., Shea, K.-S., Chen, K.-H., Lin, C.-H., et al. (2020). Magnetic properties of sedimentary smythite ($Fe_9S_{11}$). *Journal of Geophysical Research: Solid Earth*, *125*(6), e2019JB018812. https://doi.org/10.1029/2019jb018812

Housen, B. A., Banerjee, S. K., & Moskowitz, B. M. (1996). Low-temperature magnetic properties of siderite and magnetite in marine sediments. *Geophysical Research Letters*, *23*(20), 2843–2846. https://doi.org/10.1029/96gl01197

Hunt, C. P., Moskowitz, B. M., & Banerjee, S. K. (1995). Magnetic properties of rocks and minerals. In *Rock physics and phase relations. A handbook of physical constants* (Vol. 3, pp. 189–204). AGU Reference Shelf, American Geophysical Union.

Hurlbut, C. S., Jr. (1971). *Dana's manual of mineralogy* (18th ed.). John Wiley & Sons.

Hus, J. J. (1990). The magnetic properties of siderite concretion and the CRM of their oxidation products. *Physics of the Earth and Planetary Interiors*, *63*(1–2), 41–57. https://doi.org/10.1016/0031-9201(90)90058-6

Jacobs, I. S. (1963). Metamagnetism of siderite ($FeCO_3$). *Journal of Applied Physics*, *34*(4), 1106–1107. https://doi.org/10.1063/1.1729389

JCPDS–International Centre for Diffraction Data. (1993). *Mineral powder diffraction file: Databook* (782 pp.).

Jönsson, J., & Sherman, D. M. (2008). Sorption of As (III) and As (V) to siderite, green rust (fougerite) and magnetite: Implications for arsenic release in anoxic groundwaters. *Chemical Geology*, *255*(1–2), 173–181. https://doi.org/10.1016/j.chemgeo.2008.06.036

Kars, M., Aubourg, C., & Pozzi, J.-P. (2011). Low temperature magnetic behaviour near 35 K in unmetamorphosed claystones. *Geophysical Journal International*, *186*(3), 1029–1035. https://doi.org/10.1111/j.1365-246x.2011.05121.x

Morera-Chavarría, A., Griffioen, J., & Behrends, T. (2016). Optimized sequential extraction for carbonates: Quantification and $\delta^{13}C$ analysis of calcite, dolomite and siderite. *Chemical Geology*, *443*, 146–157. https://doi.org/10.1016/j.chemgeo.2016.09.025

Mørk, M. B., McEnroe, S. A., & Olesen, O. (2002). Magnetic susceptibility of mesozoic and cenozoic sediments off mid Norway and the role of siderite: Implications for interpretation of high-resolution aeromagnetic anomalies. *Marine and Petroleum Geology*, *19*(9), 1115–1126. https://doi.org/10.1016/s0264-8172(02)00115-0

Pekov, I. V., Perchiazzi, N., Merlino, S., Kalachev, V. N., Merlini, M., & Zadov, A. E. (2007). Chukanovite, $Fe_2(CO_3)(OH)_2$, a new mineral from the weathered iron meteorite Dronino. *European Journal of Mineralogy*, *19*(6), 891–898. https://doi.org/10.1127/0935-1221/2007/0019-1767

Postma, D. (1981). Formation of siderite and vivianite and the pore-water composition of a recent bog sediment in Denmark. *Chemical Geology*, *31*, 225–244. https://doi.org/10.1016/0009-2541(80)90088-1

Poulton, S. W., & Canfield, D. E. (2005). Development of a sequential extraction procedure for iron: Implications for iron partitioning in continentally derived particulates. *Chemical Geology*, *214*(3–4), 209–221. https://doi.org/10.1016/j.chemgeo.2004.09.003

Roberts, A. P. (2015). Magnetic mineral diagenesis. *Earth-Science Reviews*, *151*, 1–47. https://doi.org/10.1016/j.earscirev.2015.09.010

Roberts, A. P., Chang, L., Rowan, C. J., Horng, C.-S., & Florindo, F. (2011). Magnetic properties of sedimentary greigite ($Fe_3S_4$): An update. *Reviews of Geophysics*, *49*(1), RG1002. https://doi.org/10.1029/2010rg000336

Rochette, P. (1988). Inverse magnetic fabric in carbonate-bearing rocks. *Earth and Planetary Science Letters*, *90*(2), 229–237. https://doi.org/10.1016/0012-821x(88)90103-3

Rochette, P., Fillion, G., Mattei, J. L., & Dekkers, M. J. (1990). Magnetic transition at 30-34 K in $Fe_7S_8$: Insight into a widespread occurrence of pyrrhotite in rocks. *Earth and Planetary Science Letters*, *98*(3–4), 319–328. https://doi.org/10.1016/0012-821x(90)90034-u

Rochette, P., Jackson, M., & Aubourg, C. (1992). Rock magnetism and the interpretation of anisotropy of magnetic susceptibility. *Reviews of Geophysics*, *30*(3), 209–226. https://doi.org/10.1029/92rg00733

Romanek, C. S., Jiménez-López, C., Navarro, A. R., Sánchez-Román, M., Sahai, N., & Coleman, M. (2009). Inorganic synthesis of Fe–Ca–Mg carbonates at low temperature. *Geochimica et Cosmochimica Acta*, *73*(18), 5361–5376. https://doi.org/10.1016/j.gca.2009.05.065

Saunders, J. A., & Swann, C. T. (1992). Nature and origin of authigenic rhodochrosite and siderite from the Paleozoic aquifer, northeast Mississippi, USA. *Applied Geochemistry*, *7*(4), 375–387. https://doi.org/10.1016/0883-2927(92)90027-z

Seguin, M. (1966). Instability of $FeCO_3$ in air. *American Journal of Science*, *264*(7), 562–568. https://doi.org/10.2475/ajs.264.7.562

Senftle, F. E., Thorpe, A. N., Briggs, C., Alexander, C., Minkin, J., & Griscom, D. L. (1975). The Néel transition and magnetic properties of terrestrial, synthetic, and lunar ilmenites. *Earth and Planetary Science Letters*, *26*(3), 377–386. https://doi.org/10.1016/0012-821x(75)90014-x

Sitko, R., Zawisza, B., Krzykawski, T., & Malicka, E. (2009). Determination of chemical composition of siderite in concretions by wavelength-dispersive X-ray spectrometry following selective dissolution. *Talanta*, *77*(3), 1105–1110. https://doi.org/10.1016/j.talanta.2008.08.019

Stookey, L. L. (1970). Ferrozine – A new spectrophotometric reagent for iron. *Analytical Chemistry*, *42*(7), 779–781. https://doi.org/10.1021/ac60289a016

Viollier, E., Inglett, P. W., Hunter, K., Roychoudhury, A. N., & Van Cappellen, P. (2000). The ferrozine method revisited: Fe (II)/Fe (III) determination in natural waters. *Applied Geochemistry*, *15*(6), 785–790. https://doi.org/10.1016/s0883-2927(99)00097-9

Wiesli, R. A., Beard, B. L., & Johnson, C. M. (2004). Experimental determination of Fe isotope fractionation between aqueous Fe (II), siderite and "green rust" in abiotic systems. *Chemical Geology*, *211*(3–4), 343–362. https://doi.org/10.1016/j.chemgeo.2004.07.002

Zergenyi, R. S., Hirt, A. M., Zimmermann, S., Dobson, J. P., & Lowrie, W. (2000). Low-temperature magnetic behavior of ferrihydrite. *Journal of Geophysical Research*, *105*(B4), 8297–8303. https://doi.org/10.1029/1999jb900315

## References From the Supporting Information

Spassov, S., & Egli, R. (2016). Method for correcting remanent fields in magnetic property measurement systems without field compensation. Technical note of Working Group 2, COST Action Radiomag, TD1402 (pp. 13).

Takanashi, K., Kurokawa, H., & Fujimori, H. (1993). A novel hysteresis loop and indirect exchange coupling in Co/Pt/Gd/Pt multilayer films. *Applied Physics Letters*, *63*(11), 1585–1587. https://doi.org/10.1063/1.110756